JGR Space Physics

RESEARCH ARTICLE
10.1029/2022JA030540

Geomagnetic Detection of the Atmospheric Acoustic Resonance at 3.8 mHz During the Hunga Tonga Eruption Event on 15 January 2022

Yosuke Yamazaki[1], Gabriel Soares[2], and Jürgen Matzka[3]

[1]Leibniz Institute of Atmospheric Physics at the University of Rostock, Kühlungsborn, Germany, [2]Observatório Nacional, Rio de Janeiro, Brazil, [3]GFZ German Research Centre for Geosciences, Potsdam, Germany

Key Points:

- The effect of the January 2022 Hunga Tonga-Hunga Ha'apai volcano eruption on the geomagnetic field is examined
- Geomagnetic oscillation with a frequency of ~3.8 mHz is observed simultaneously near the volcano and its magnetic conjugate point
- The oscillation is attributed to the acoustic resonance of the atmosphere

Correspondence to:
Y. Yamazaki,
yamazaki@iap-kborn.de

Citation:
Yamazaki, Y., Soares, G., & Matzka, J. (2022). Geomagnetic detection of the atmospheric acoustic resonance at 3.8 mHz during the Hunga Tonga eruption event on 15 January 2022. *Journal of Geophysical Research: Space Physics*, *127*, e2022JA030540. https://doi.org/10.1029/2022JA030540

Received 8 APR 2022
Accepted 22 JUN 2022

Abstract Modeling studies have predicted that the acoustic resonance of the atmosphere during geophysical events such as earthquakes and volcanos can lead to an oscillation of the geomagnetic field with a frequency of about 4 mHz. However, observational evidence is still limited due to scarcity of suitable events. On 15 January 2022, the submarine volcano Hunga Tonga-Hunga Ha'apai (20.5°S, 175.4°W, Tonga) erupted in the Pacific Ocean and caused severe atmospheric disturbance, providing an opportunity to investigate geomagnetic effects associated with acoustic resonance. Following the eruption, geomagnetic oscillation is observed at Apia, approximately 835 km from Hunga Tonga, mainly in the Pc 5 band (150–600 s, or 1.7–6.7 mHz) lasting for about 2 hr. The dominant frequency of the oscillation is 3.8 mHz, which is consistent with the frequency of the atmospheric oscillation due to acoustic resonance. The oscillation is most prominent in the eastward (Y) component, with an amplitude of ~3 nT, which is much larger than those previously reported for other events (<1 nT). Comparably large oscillation is not found at other stations located further away (>2700 km). However, geomagnetic oscillation with a much smaller amplitude (~0.3 nT) is observed at Honolulu, which is located near the magnetic conjugate point of Hunga Tonga, in a similar wave form as at Apia, indicating interhemispheric coupling. This is the first time that geomagnetic oscillations due to the atmospheric acoustic resonance are simultaneously detected at magnetic conjugate points.

1. Introduction

Geophysical events such as earthquakes, volcanoes and tsunamis can cause atmospheric waves such as acoustic waves and gravity waves (Yeh & Liu, 1974). Acoustic waves have frequencies higher than the acoustic cutoff frequency (~3.2 mHz at the stratopause), while gravity waves have frequencies lower than the Brunt-Väisälä frequency (~2.7 mHz at the stratopause). They can propagate away from the source, transferring energy and momentum into the middle and upper atmosphere. As the waves propagate to higher altitudes, they grow in amplitude due to decreasing atmospheric density. Yeh and Liu (1974) estimated that a seismic wave with vertical ground displacement of 5 mm could lead to an acoustic wave whose vertical wind velocity reaches 30 m/s at an altitude of 150 km. Such a large perturbation of the neutral atmosphere would have a significant impact on the dynamics and electrodynamics of the ionosphere. Indeed, ionospheric disturbances associated with acoustic and gravity waves have been reported following strong earthquakes and other geophysical events for many decades (see reviews by e.g., Astafyeva, 2019; Meng et al., 2019).

Atmospheric oscillations with frequencies near the acoustic cutoff frequency are frequently observed after eruption events (Kanamori et al., 1994). Modeling studies have shown that those oscillations can be explained by acoustic waves trapped between the ground and thermosphere (e.g., Lognonné et al., 1998; Matsumura et al., 2011, 2012; Shinagawa et al., 2007; Tahira, 1995). For example, Matsumura et al. (2012) used a non-hydrostatic model to examine the atmospheric response to an impulsive point source on the ground. According to their simulations, atmospheric disturbance propagates vertically upward and reaches the ionosphere (>100 km) above the source within 10 min. The atmospheric oscillation initially contains various frequencies at 2–5 mHz (periods about 3–8 min) but gradually, the acoustic resonance frequency at ~3.7 mHz (4.5 min) becomes predominant and lasts for about 2 hours. Ionospheric oscillations around those frequencies have been observed following earthquakes and volcanic eruptions (e.g., Choosakul et al., 2009; Dautermann et al., 2009; Heki et al., 2006; Nakashima et al., 2016; Saito et al., 2011).

At heights of the ionospheric E region (ca 100–150 km, also known as the dynamo region), ions move with neutral air while the motion of electrons is controlled by the ambient magnetic field. The difference in the motions of the ions and electrons lead to electric fields and currents. The production mechanism of electromagnetic fields in the ionosphere by neutral winds is known as the ionospheric wind dynamo (Richmond, 1995). The strength of the ionospheric dynamo currents depends on the neutral wind velocity as well as plasma density. Under normal quiet conditions at mid latitudes, tidal motion of the neutral air with the velocity of 40–60 m/s can drive ionospheric currents on the order of 10 mA/m, which in turn produce magnetic field variations of a few 10s nT on the ground (Yamazaki & Maute, 2017). Atmospheric disturbance caused by volcanic eruptions and other geophysical events can result in the modulation of those ionospheric dynamo currents and hence magnetic field variation.

Studies found evidence for geomagnetic variation associated with acoustic waves following geophysical events. For instance, Iyemori et al. (2005) observed oscillation of the geomagnetic field at a period of 3.6 min (4.6 mHz) following the December 2004 Sumatra earthquake. The oscillation with an amplitude of ∼0.5 nT was detected at a ground station approximately 1500 km away from the epicenter, but not at other stations located further away. Aoyama et al. (2016) observed geomagnetic oscillations at 3.6 and 4.3 min (4.7 and 3.8 mHz, respectively) after the Calbuco volcano eruption in April 2015. The amplitude of the oscillation was ∼0.2 nT at Huancayo, located approximately 3200 km away from the volcano. Aoyama et al. (2016) also used magnetometer data from a low Earth orbit satellite Swarm, and found magnetic field variations not only over the Calbuco volcano but also near the magnetic conjugate point. Their results implied that electromagnetic fields locally generated by acoustic waves can be instantly transferred to its magnetic conjugate point along equipotential magnetic field lines. However, it took approximately 15 min for the Swarm satellite to fly from the latitude of the volcano to its magnetic conjugate point, and thus simultaneous detection of magnetic field variations at the magnetic conjugate point is yet to be achieved. Hasbi et al. (2009) noted geomagnetic oscillation at a period of 4.8 min (3.5 mHz) following the March 2005 Sumatra earthquake. The oscillation with an amplitude of ∼0.2 nT was detected at a station approximately 450 km away from the epicenter, but not at other stations that are more than 2300 km away. All these studies suspected that the observed geomagnetic oscillations resulted from ionospheric currents driven by acoustic waves.

The impact of acoustic waves on the ionosphere and geomagnetic field was evaluated in a series of modeling studies by Zettergren and Snively (2013, 2015, 2019). It was demonstrated that acoustic waves can drive ionospheric currents and cause magnetic field variation, which oscillate at the frequency of the driving acoustic waves. According to their work, the ionospheric currents in the direction perpendicular to the ambient magnetic field are mainly localized near the source region (within approximately ±5° in longitude and latitude), while the currents parallel to the magnetic field lines extend away from the source region into the magnetic conjugate point in the opposite hemisphere. The field-aligned currents close the perpendicular currents so that the total currents will be divergence-free. As a result, a three-dimensional electric current system is formed, which is elongated along the magnetic flux tube. Associated ground magnetic field variations are mainly localized near the source, but can also be observed near the magnetic conjugate point with smaller amplitude. Near the source, the amplitude of the geomagnetic variation can be as large as 1.5 nT, for the case of the 2011 M9.0 Tohoku earthquake (Zettergren & Snively, 2019).

While the main features of geomagnetic variation caused by acoustic waves are well described in the modeling studies by Zettergren and Snively (2013, 2015, 2019), observational evidence to support and compare with the numerical predictions is still limited. This is due to scarcity of suitable events, in which atmospheric disturbance is strong enough to drive ionospheric dynamo currents and also in which a magnetometer is conveniently located near the source and/or its magnetic conjugate point. On 15 January 2022, the submarine volcano Hunga Tonga-Hunga Ha'apai (20.5°S, 175.4°W, Tonga) erupted in the Pacific Ocean at 04:14:45 UT (Yuen et al., 2022). Early images from a meteorological satellite revealed the formation of large cloud reaching 30 km in height and 400 km in diameter (Smart, 2022), indicating severe atmospheric disturbance. The event was also accompanied by a M5.8 earthquake and tsunami (Yuen et al., 2022). The objective of this study is to examine the possible geomagnetic effect of ionospheric dynamo currents associated with acoustic resonance during this extreme geophysical event, and compare its characteristics with those previously reported for other events (Aoyama et al., 2016; Hasbi et al., 2009; Iyemori et al., 2005) and with those predicted by numerical models (Zettergren & Snively, 2013, 2015, 2019).

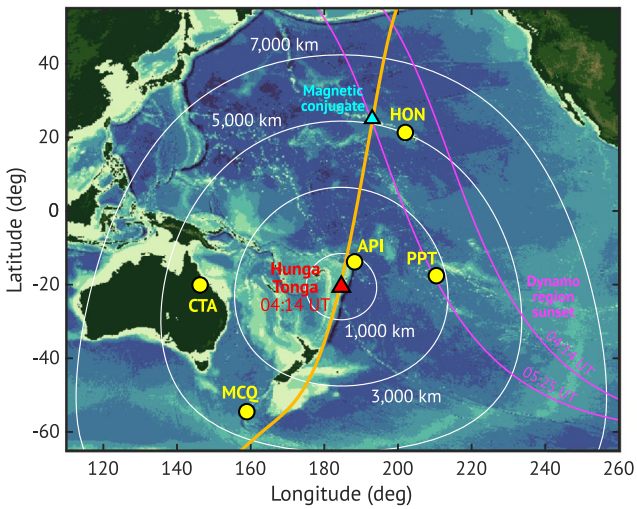

Figure 1. A map with the positions of the Hunga Tonga volcano (red triangle), its magnetic conjugate point (cyan triangle) and geomagnetic observatories (yellow circles). Curves in white show the distance from the Hunga Tonga. The orange curve indicates the magnetic meridian on which Hunga Tonga lies. The magenta lines show the location of the dynamo-region sunset terminator at 04:14 UT and 05:25 UT, which is defined by the solar zenith angle $\chi = 100°$. The dynamo region on the western side of the magenta line is before the sunset, and the dynamo region on the eastern side of this line is after the sunset. The land topography and ocean bathymetry are based on ETOPO1 (Amante & Eakins, 2009).

Variation of the geomagnetic field during the Hunga Tonga event could result not only from ionospheric dynamo currents but also from other causes. For example, tsunami waves can lead to geomagnetic variation by moving electrically conductive sea water and thus inducing electric fields and currents (e.g., Minami, 2017). Magnetic field data may also contain geomagnetic disturbance of solar wind origin and spurious magnetic field variation due to changes in the orientation of magnetometer sensors associated with ground vibration caused by seismic waves. The possible contaminations from these non-ionospheric-dynamo sources will be carefully examined and ruled out.

2. Data

Ground-based 1 Hz magnetometer data from the following geomagnetic observatories were obtained from the INTERMAGNET network (Love & Chulliat, 2013): Apia (API, 13.8°S, 171.8°W), Pamatai (PPT, 17.6°S, 149.6°W), Charters Towers (CTA, 20.1°S, 146.3°E), Honolulu (HON, 21.3°N, 158.0°W) and Macquarie Island (MCQ, 54.5°S, 159.0°E). Figure 1 shows the location of the Hunga Tonga volcano (red triangle) and the geomagnetic observatories (yellow circles). Apia is the closest observatory to Hunga Tonga, located 835 km north-northeast of the volcano. Pamatai, Charters Towers, Honolulu and Macquarie Island are neighboring observatories with respective distances to the volcano of 2730 km (east of Hunga Tonga), 3990 km (west), 4995 km (north-northeast) and 4350 km (south-southwest). Curves in white indicate the distance to Hunga Tonga. Also, the orange curve shows the magnetic meridian on which Hunga Tonga is located, with the cyan triangle indicating the location of the magnetic conjugate point of Hunga Tonga. Honolulu is located approximately 1005 km east of the magnetic conjugate point of Hunga Tonga. Macquarie Island is located in the auroral zone (64.0°S magnetic latitude), where the geomagnetic field is especially susceptible to disturbances caused by changes in the solar wind.

Other data used in this study include the Dst index, which is a measure of geomagnetic storm activity. Hourly values of the Dst index were used to evaluate storm effects on the geomagnetic field during the Hunga Tonga event. The geomagnetic activity index Hp30 (Yamazaki et al., 2022) was also used. Hp30 represents planetary geomagnetic activity in a similar way as the 3-hourly geomagnetic activity index *Kp* (Matzka et al., 2021) but with a higher time resolution of 30 min. OMNI 1-min solar wind data (King & Papitashvili, 2005) were used to demonstrate solar wind driving of geomagnetic activity. All the solar wind data were shifted by 17 min to take into account the propagation time from the bow shock to the ionosphere (Manoj et al., 2008), which facilitates the comparison between OMNI and ground-based magnetometer data. Furthermore, 1-min tide gauge data from the Apia Upolu station (13.8°S, 171.8°W) were used to evaluate the contribution of tsunami waves on magnetic field variation at Apia during the Hunga Tonga event. The Apia Upolu station is located close to the Apia magnetic observatory.

3. Results and Discussion

3.1. Localized Large Magnetic Field Variation

We first give an overview of magnetic field variations observed at different stations around the time of the Hunga Tonga event. Figures 2a–2e present the eastward (Y) component of the geomagnetic field observed at Apia, Pamatai, Honolulu, Charters Towers and Macquarie Island during the period from 12:00 UT on 14 January 2022 to 00:00 UT on 16 January. In Figures 2a–2e, the top panel shows the raw data, the middle panel shows the 5- to 600-s band pass filtered data, and the bottom panel shows the Morlet wavelet spectrum of the raw data. For the wavelet spectrum, tick marks are placed at 5, 10, 45, 150 and 600 s, which correspond to the period ranges for the magnetic pulsations Pc 2 (5–10 s, or 100–200 mHz), Pc 3 (10–45 s, or 22.2–100 mHz), Pc 4 (45–150 s, or 6.7–22.2 mHz) and Pc 5 (150–600 s, or 1.7–6.7 mHz) (e.g., McPherron, 2005; Saito, 1969). An additional tick

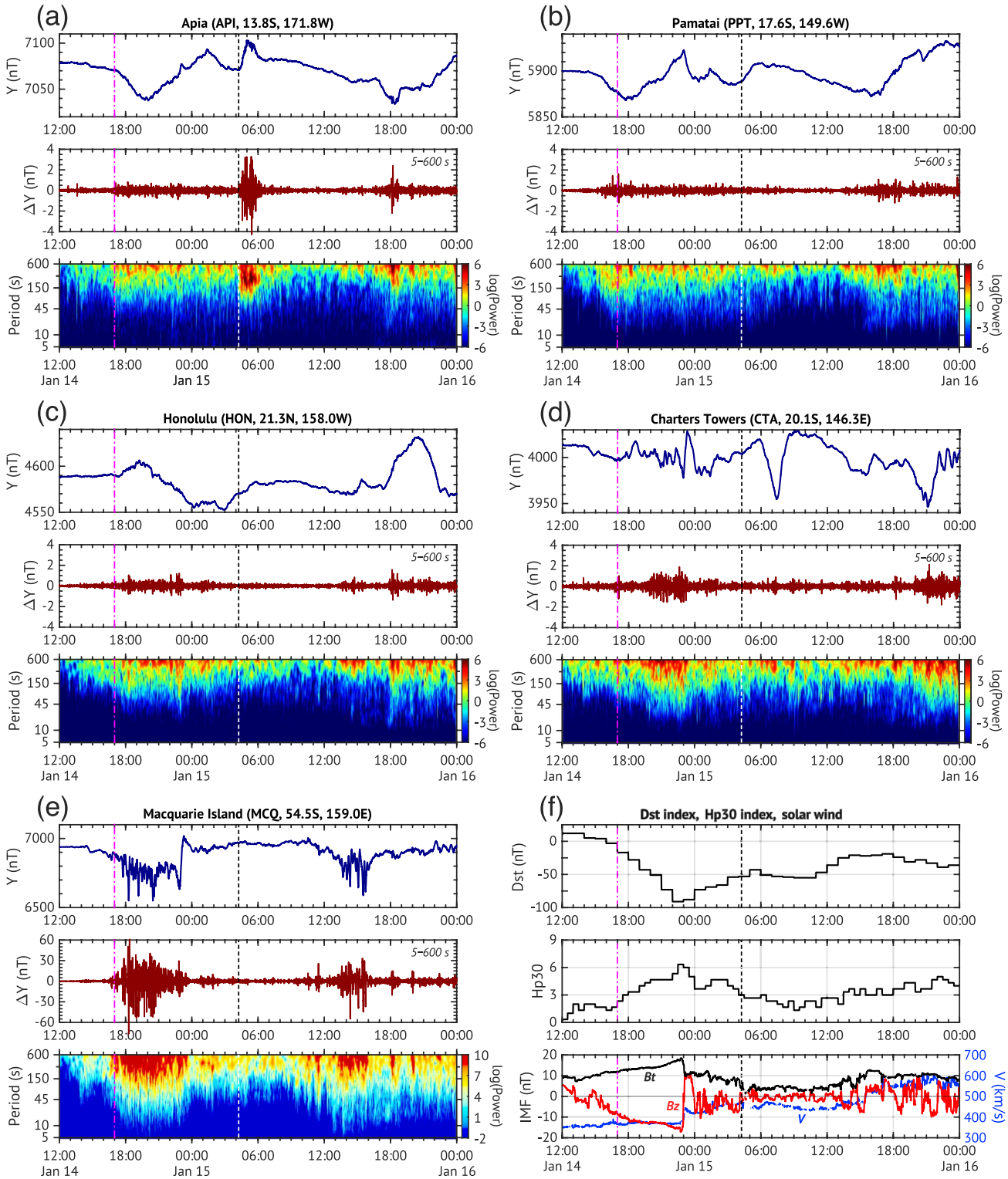

Figure 2. (a–e) (Top) the Y component of the geomagnetic field, (middle) band-pass filtered data at periods 5–600 s, and (bottom) wavelet spectrum for Apia, Pamatai, Honolulu, Charters Towers and Macquarie Island. Results for Macquarie Island are presented with different scales than those at the other stations. Vertical dash-dotted lines in magenta indicate the beginning of the geomagnetic storm, while vertical dashed lines in black/white indicate the time of the Hunga Tonga eruption. (f) (top) hourly Dst index, (middle) half-hourly Hp30 index, and (bottom) 1-min OMNI solar wind data with 17-min time shift. *Bt* (black) and *Bz* (red) are the total intensity and northward component of the interplanetary magnetic field and *V* (blue) is the solar wind speed.

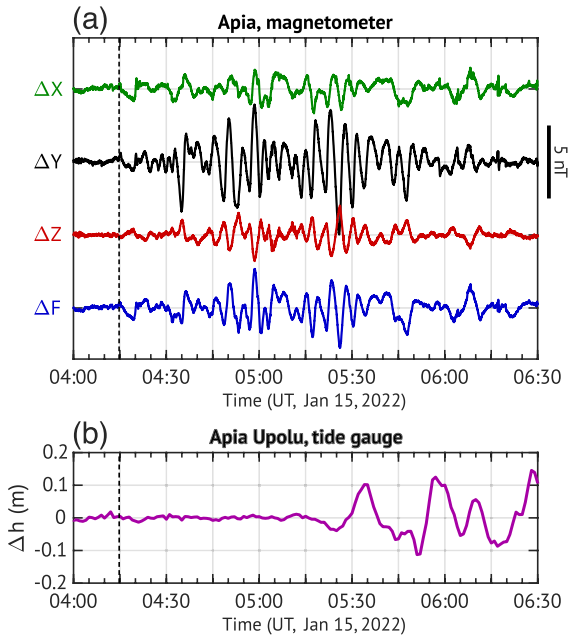

Figure 3. (a) High-pass filtered magnetometer data for Apia with a cutoff period of 20 min during 04:00–06:30 UT on 15 January 2022. (b) Same as (a) but for sea level data from the Apia Upolu tide gauge, indicating the arrival of tsunami waves around 05:30 UT. The vertical black dashed lines indicate the time of the Hunga Tonga eruption.

mark is placed at 300 s (3.3 mHz). The black/white vertical dashed lines mark the onset of the Hunga Tonga eruption at 04:14:45 UT on 15 January, while the magenta vertical dash-dotted lines show the onset of geomagnetic storm at 17:00 UT on 14 January, which is described below.

There was a geomagnetic storm on 14 January 2022, preceding the Hunga Tonga eruption by several hours. In Figure 2f a rapid decrease of the Dst index (top) and increase of the Hp30 index (middle) is observed at 17:00 UT on 14 January 2022, which is defined here as the onset of the storm. The Dst index reached a minimum value of −94 nT at 23:00 UT on 14 January and remained negative throughout the day on 15 January, indicating that the Hunga Tonga eruption occurred during the recovery phase of the storm. The bottom panel shows the total intensity (Bt) and northward component (Bz) of the IMF, and the solar wind speed (V). In general, the energy transfer from the solar wind to the magnetosphere is more efficient for larger values of Bt and V, and for a negative value of Bz (e.g., Akasofu, 1981; Lockwood, 2022). It is clear from Figure 2f that the geomagnetic storm starting at 17:00 UT was mainly driven by the long-lasting strong IMF containing large negative Bz around 17:00–24:00 UT on 14 January. The IMF was weak from 04:10 UT to 13:10 UT on 15 January, indicating that the magnetosphere was only weakly driven by the solar wind at the time of the Hunga Tonga eruption and in the following hours. The Hp30 index was equal to or less than 3 during 04–13 UT, confirming that planetary geomagnetic activity was low during the Hunga Tonga event.

The wavelet spectrum in Figure 2a reveals an enhancement of the magnetic field variation in the Pc5 range (150–600 s, or 1.7–6.7 mHz) at Apia shortly after the Hunga Tonga eruption. The enhanced geomagnetic variation lasted for approximately 2 hr until about 06:00 UT, under low geomagnetic activity conditions. The amplitude of the variation exceeds 3 nT. In contrast to this, there is no clear indication of enhanced magnetic field variation in the Pc 5 band at other observatories (Figures 2a–2e) following the Hunga Tonga eruption. An overall enhancement in the power of Pc 3–5 magnetic pulsations is seen at all the stations following the geomagnetic storm, most profoundly at Macquarie Island in the auroral zone. Enhanced magnetic pulsation activity is also seen toward the end of 15 January due to the high speed solar wind. A transient magnetic disturbance is observed at all the stations around 18:00 UT on 15 January, that could be a Pi 2 pulsation associated to substorm activity. All these results suggest that the large geomagnetic variation, ∼3 nT, observed in the Pc 5 band at Apia after the Hunga Tonga eruption is localized and easily distinguishable from geomagnetic disturbance of solar wind origin, which is globally observed and most prominent at high latitudes.

3.2. Effects of Tsunami and Artefact Due To Ground Shaking

Next, we take a closer look at the wave form of the geomagnetic oscillation observed at Apia following the Hunga Tonga eruption. Figure 3a shows high-pass filtered magnetometer data at Apia with a cut-off period of 20 min in the northward (X), eastward (Y), vertical (Z) components and in the total intensity (F) during the period 04:00–06:30 UT on 15 January 2022. The vertical dashed line indicates the time of the eruption. 10 minutes after the eruption, at 04:25 UT, pulsation-like oscillations are already visible in the Y component. The oscillation is seen to continue until around 06:00 UT. The magnetic field in the Z component shows a similar oscillation as in the Y component, but the amplitude is approximately half and is in opposite phase. Oscillations in the X component are less clear.

Corresponding high-pass filtered data from the tide gauge at Apia Upolu is shown in Figure 3b. The tsunami waves arrived at Apia Upolu around 05:30 UT, which is almost 1 hour after the start of the geomagnetic variation at Apia around 04:25 UT. Previous studies have shown that magnetic field variation related to tsunami waves starts nearly at the same time as the arrival of the tsunami waves (e.g., Manoj et al., 2011; Schnepf et al., 2016). The tsunami-related geomagnetic variation in the horizontal component is expected to be very small at a land

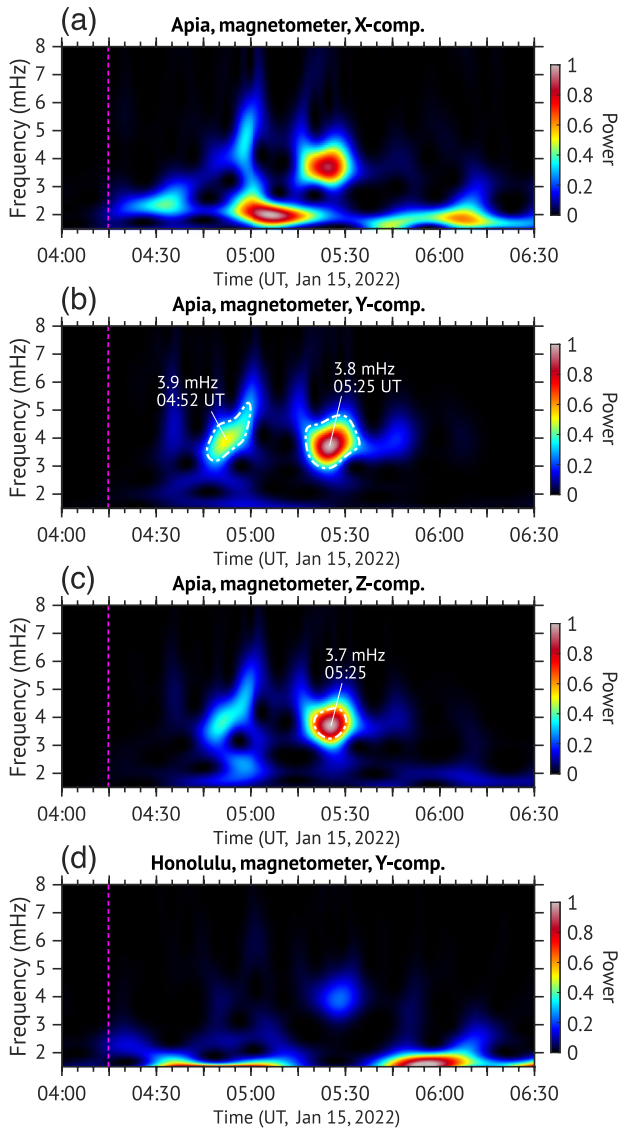

Figure 4. Wavelet spectra over the frequency range of 1.5–8 mHz for the X, Y and Z components of the geomagnetic field at Apia and for the Y component of the geomagnetic field at Honolulu. The power is normalized to the maximum value. The 95% significance level is indicated by white dash-dotted curves. The vertical magenta lines show the onset of the Hunga Tonga eruption.

observatory like Apia, and the variation in the Z component is expected to have a wave form similar to that of the variation in the sea level (e.g., Lin et al., 2021; Minami et al., 2015). In Figure 3, however, magnetic field variation is larger in the Y component than in the Z component, and there is no similarity between the variations in the Z component and sea level. These results rule out the ocean dynamo by tsunami waves (Minami, 2017) as the main mechanism for the geomagnetic variation observed at Apia following the Hunga Tonga eruption.

It is noted that tsunami waves could still contribute to geomagnetic variation through the ionospheric wind dynamo. Vertical displacement of the sea surface by tsunami waves can lead to acoustic waves in the atmosphere (Inchin et al., 2020), which can drive ionospheric currents and produce magnetic field variation (Sorokin & Yaschenko, 2021). Effects of ionospheric currents will be discussed in Section 3.3.

Seismic waves generated by the Hunga Tonga eruption have been observed globally (Yuen et al., 2022). Ground motion due to the seismic waves could affect the orientation of the fluxgate sensors that measure the geomagnetic vector components and thus introduce spurious variation in X, Y and Z. The total field $F = (X^2 + Y^2 + Z^2)^{0.5}$ calculated from the vector components is far less susceptible to ground motion as it is invariant to sensor orientation. Additionally, the total field F can be measured by an overhauser magnetometer, which is also less susceptible to ground motion effects because its measurement principle does not require any specific sensor orientation. In Figures 3a and 3f data come from an overhauser magnetometer, and it shows pulsation-like disturbance similar to that in the Y and Z components, confirming that the geomagnetic disturbance observed at Apia after the Hunga Tonga eruption is not an artefact due to ground shaking. Total field F values calculated from the vector components present nearly identical variations (not shown here), leading to the same conclusion.

3.3. Effects of Ionospheric Dynamo Currents

We now consider ionospheric dynamo currents as a possible source of the geomagnetic variation observed at Apia following the Hunga Tonga eruption. As mentioned earlier, atmospheric waves caused by a surface disturbance can reach the dynamo region above the source within 10 min (e.g., Matsumura et al., 2012). This enables the fast response of the ionosphere, and hence geomagnetic field, to the volcanic eruption as seen in Figure 3. A condition that needs to be satisfied for the ionospheric wind dynamo to be effective is that the dynamo region receives the sunlight so that ionospheric plasma density is sufficiently high to support electric currents. The solar zenith angle (χ) at the location of Hunga Tonga remained below 100° during 04:00–06:30 UT (16:18–18:48 LT), indicating that the dynamo region was on the sunlit side (see also Figure 1). This makes it possible for atmospheric waves excited by the Hunga Tonga eruption to modulate ionospheric dynamo currents.

Figures 4a–4c present wavelet spectra for the oscillation of the geomagnetic field over the frequency range of 1.5–8 mHz (around the Pc 5 band, 1.7–6.7 mHz) in the X, Y and Z components observed at Apia following the Hunga Tonga eruption. For the Y and Z components, spectral peaks around 3.8 mHz are above the 95% significance level (dash-dotted curves in white). The dominant frequency at ~3.8 mHz is consistent with the atmospheric oscillation due to acoustic waves trapped between the ground and thermosphere, or acoustic resonance at 3.6–4.0 mHz (e.g., Lognonné et al., 1998; Matsumura et al., 2011, 2012; Shinagawa et al., 2007; Tahira, 1995). There are two bursts of the 3.8-mHz geomagnetic oscillation; the first one is around 04:52 UT and the second one is around 05:25 UT. They might involve different mechanisms to drive acoustic resonance. More studies are

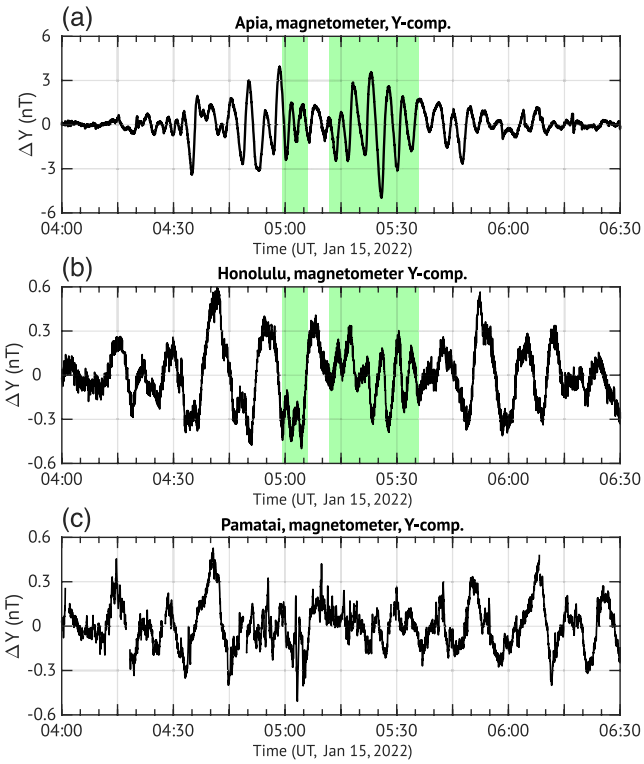

Figure 5. High-pass filtered magnetic field data in the Y component for Apia, Honolulu and Pamatai with a cut-off period of 20 min. Shading in green indicates the time interval where the wave form of ΔY at Honolulu resembles that at Apia.

necessary to explain the two bursts of the 3.8-mHz geomagnetic oscillation. In Figure 4a, a spectral peak at ~3.8 mHz is also visible in the X component around 05:25 UT, but is below the 95% significance level due to its small variation (see also Figure 3a).

Evidence for conjugate effect is presented in Figure 5. Figure 5a shows high-pass filtered magnetometer data in the Y component at Apia with a cut-off period of 20 min, that is, the same as ΔY in Figure 3a. Figure 5b depicts ΔY for Honolulu, which is approximately 1005 km away from the magnetic conjugate point of Hunga Tonga (see Figure 1). ΔY at Honolulu shows similar variation as ΔY at Apia, especially during the second burst of the 3.8-mHz geomagnetic oscillation around 05:25 UT. Such agreement is not clearly visible between ΔY at Apia and Pamatai (Figure 5c), although Pamatai is located closer to Apia than Honolulu is. Although not presented here, variations in the X and Z components at Honolulu are not similar to the variations in the corresponding components at Apia. During the 3.8-mHz geomagnetic oscillation around 05:25 UT, ΔY at Honolulu and Apia are in opposite phase (Figures 5a and 5b), and the amplitude of the oscillation at Honolulu is approximately one tenth that of ΔY at Apia. The small variation is the reason why the 3.8-mHz geomagnetic oscillation at Honolulu is not well resolved in the wavelet spectrum in Figure 2c. A close inspection of the wavelet spectrum for Y at Honolulu (Figure 4d) reveals a peak at ~3.8 mHz around 05:25 UT but below the 95% significance level. Nevertheless, the geomagnetic oscillation at Honolulu, which is similar but smaller than that at Apia, is in agreement with the numerical prediction of the magnetic field variation at magnetic conjugate point (Zettergren & Snively, 2019). As indicated in Figure 1, the magnetic conjugate point of Hunga Tonga was around the dynamo-region sunset at 05:25 UT. Thus, the E-region plasma density at the magnetic conjugate point is expected to be substantially lower than at Hunga Tonga. Such a hemispheric asymmetry in the plasma density can result in a hemispheric asymmetry of ionospheric currents as pointed out by Zettergren and Snively (2013), which would be part of the reason why the geomagnetic oscillation at Honolulu is much smaller than that at Apia.

As shown in Figure 3a, the geomagnetic oscillation at Apia is most prominent in the Y component, and thus can be attributed to electric currents mainly in the north-south direction. For example, field-aligned currents would produce ground magnetic field variation mainly in the Y component. Magnetic field variation in the Z component is absent right below the field-aligned currents, but non-zero at either the eastern or western side of the currents. Since Apia is located about 100 km east to the magnetic meridian of Hunga Tonga (Figure 1), northward/upward field-aligned currents over Hunga Tonga would generate a negative perturbation in the Y component and a positive perturbation in the Z component. This can explain why the magnetic field variations at Apia in the Y and Z components are in opposite phase (Figure 3a). The same currents would also produce a negative perturbation in the Y component at Honolulu. However, as shown in Figures 5a and 5b, the Y-component geomagnetic oscillations at Apia and Honolulu are in opposite phase. One possible explanation is that ΔY at Apia and Honolulu are produced by electric currents flowing along different magnetic field lines. Modeling work is needed to determine the spatial structure of the electric current system responsible for the geomagnetic oscillations observed during the Hunga Tonga event.

The amplitude of the geomagnetic oscillation at Apia during the Hunga Tonga event is approximately 3 nT. This is much larger than those previously reported for other events (e.g., Aoyama et al., 2016; Hasbi et al., 2009; Iyemori et al., 2005), which are less than 1 nT. It is also larger than the maximum geomagnetic variation (~1.5 nT) numerically predicted for the 2011 Tohoku earthquake (Zettergren & Snively, 2019). More modeling work is needed to assess the full extent of geomagnetic effects during the Hunga Tonga event and identify the cause of exceptionally large geomagnetic oscillation.

4. Summary and Conclusions

The Hunga Tonga-Hunga Ha'apai volcano in the Pacific Ocean erupted on 15 January 2022. Less than 10 min after the eruption, magnetic field variation started at the geomagnetic observatory Apia, approximately 835 km from Hunga Tonga, and lasted for about 2 hr. The variation is observed mainly in the eastward (Y) component within the Pc 5 band (150–600 s, or 1.7–6.7 mHz) with an amplitude of ∼3 nT. Such a large enhancement in the Pc 5 band is not seen at other observatories located more than 2700 km away, including a station in the auroral region where the geomagnetic field is more susceptible to disturbances associated with solar wind variations. This excludes the contribution of solar wind variations as the main cause of the Pc 5 oscillation of the geomagnetic field at Apia. The contribution of ocean dynamo by tsunami waves is also excluded, because the oscillation of the geomagnetic field started earlier than the arrival of the tsunami waves by almost 1 hour. The geomagnetic oscillation at Apia is also evident in the total intensity (F), which is far less susceptible to ground motion than the Y component. Thus, the geomagnetic oscillation is not spurious variation due to ground shaking caused by seismic waves.

The geomagnetic variation at Apia is most likely due to ionospheric dynamo currents driven by the acoustic resonance of the atmosphere. The following is the summary of the results that support our interpretation:

1. The large geomagnetic oscillation (∼3 nT) is localized near the volcano, which is qualitatively consistent with the model prediction by Zettergren and Snively (2019).
2. The geomagnetic oscillation lasted for about 2 hours, which is consistent with the duration of atmospheric oscillation caused by an impulsive point source on the ground (Matsumura et al., 2012).
3. The dominant frequency of the geomagnetic oscillation is 3.8 mHz, which is in agreement with the known frequency of the atmospheric acoustic resonance between the ground and thermosphere (e.g., Inchin et al., 2020; Kanamori et al., 1994; Lognonné et al., 1998; Matsumura et al., 2012, 2011; Shinagawa et al., 2007; Tahira, 1995).
4. The geomagnetic oscillation is detected at Honolulu near the magnetic conjugate point in a similar wave form but with a smaller amplitude, which is consistent with the model prediction by Zettergren and Snively (2019). This is the first time that geomagnetic oscillations associated with acoustic resonance are detected simultaneously near the source and its magnetic conjugate point.

Concerning the conjugate effect, the amplitude of the Y-component geomagnetic oscillation at Honolulu is about one tenth that at Apia, and the phase of the oscillation at Honolulu is opposite to that at Apia. Modeling studies are needed to understand the three-dimensional structure of the ionospheric current system caused by the Hunga Tonga event.

Data Availability Statement

The geomagnetic data used in this paper are available at the INTERMAGNET website (https://www.intermagnet.org/data-donnee/download-eng.php). ETOPO1 Global Relief Model is available at the NOAA website (https://www.ngdc.noaa.gov/mgg/global/); see also data publication (NOAA National Geophysical Data Center, 2009). The Dst index is available at the website of the World Data Center for Geomagnetism, Kyoto (http://wdc.kugi.kyoto-u.ac.jp/dstae/index.html); see also data publication (Nose et al., 2015). The Hp30 index is available at the website of Deutsches GeoForschungsZentrum (GFZ) (https://www.gfz-potsdam.de/en/hpo-index); see also data publication (Matzka et al., 2022). The 1-min solar wind data are available from the OMNIWeb (https://omniweb.gsfc.nasa.gov/form/omni_min.html); see also data publication (Papitashvili & King, 2020). The sea level data for Apia Upolu on 15 January 2022 are available at the IOC website (https://www.ioc-sealevelmonitoring.org/bgraph.php?code=upol&output=tab&period=1&endtime=2022-01-16); see also data publication (Flanders Marine Institute (VLIZ); Intergovernmental Oceanographic Commission (IOC), 2021). Wavelet software used in this study is available at (https://paos.colorado.edu/research/wavelets/); see also Torrence and Compo (1998).

Acknowledgments
We thank Dr. Takuto Minami and the anonymous reviewer for assessing earlier version of the manuscript (https://doi.org/10.1002/essoar.10510482.1), which is available online since 12 February 2022. The results presented in this paper are based on the long-term observations made at geomagnetic observatories and tide gauges. We acknowledge the Ministry of Natural Resources & Environment—Meteorology Division (MNRE), Samoa, and GNS Science, New Zealand for operating API and ETH Zurich, Switzerland, the United States Geological ServicelUnited States Geological Survey (USGS) and GFZ Potsdam for supporting it. We thank Institut de Physique du Globe de Paris (IPGP) for operating PPT, the USGS for operating HON and Geoscience Australia for operating CTA and MCQ. INTERMAGNET is acknowledged for promoting high standards of geomagnetic observatory practice. We thank the geomagnetic observatories (Kakioka [JMA], Honolulu and San Juan [USGS], Hermanus [RSA], Alibag [IIG]), NiCT, and many others for their cooperation to make the real-time (quicklook) Dst index available. We acknowledge the Sea Level Station Monitoring Facility of the IOC for providing sea water level data. We also acknowledge the IRIS for making the seismic information available. G. Soares was supported by the Coordenação de Aperfeiçoamento de Pessoal de Nível Superior—Brasil (CAPES)—Finance Code 1799579. Y. Yamazaki was supported by the Deutsche Forschungsgemeinschaft (DFG) grant YA-574-3-1. J. Matzka was supported by DFG (grant MA-2578-4-1) in the framework of Priority Program 1788 "DynamicEarth." Open Access funding enabled and organized by Projekt DEAL.

References

Akasofu, S.-I. (1981). Energy coupling between the solar wind and the magnetosphere. *Space Science Reviews*, *28*(2), 121–190. https://doi.org/10.1007/bf00218810

Amante, C., & Eakins, B. W. (2009). ETOPO1 arc-minute global relief model: Procedures, data sources and analysis.

Aoyama, T., Iyemori, T., Nakanishi, K., Nishioka, M., Rosales, D., Veliz, O., & Safor, E. V. (2016). Localized field-aligned currents and 4-min TEC and ground magnetic oscillations during the 2015 eruption of Chile's Calbuco volcano. *Earth Planets and Space*, *68*(1), 1–9. https://doi.org/10.1186/s40623-016-0523-0

Astafyeva, E. (2019). Ionospheric detection of natural hazards. *Reviews of Geophysics*, *57*(4), 1265–1288. https://doi.org/10.1029/2019rg000668

Choosakul, N., Saito, A., Iyemori, T., & Hashizume, M. (2009). Excitation of 4-min periodic ionospheric variations following the great Sumatra-Andaman earthquake in 2004. *Journal of Geophysical Research*, *114*(A10). https://doi.org/10.1029/2008ja013915

Dautermann, T., Calais, E., Lognonné, P., & Mattioli, G. S. (2009). Lithosphere–atmosphere–ionosphere coupling after the 2003 explosive eruption of the Soufriere Hills Volcano, Montserrat. *Geophysical Journal International*, *179*(3), 1537–1546. https://doi.org/10.1111/j.1365-246x.2009.04390.x

Flanders Marine Institute (VLIZ); Intergovernmental Oceanographic Commission (IOC). (2021). Sea level station monitoring facility [dataset]. VLIZ. https://doi.org/10.14284/482

Hasbi, A. M., Momani, M. A., Ali, M. A. M., Misran, N., Shiokawa, K., Otsuka, Y., & Yumoto, K. (2009). Ionospheric and geomagnetic disturbances during the 2005 Sumatran earthquakes. *Journal of Atmospheric and Solar-Terrestrial Physics*, *71*(17–18), 1992–2005. https://doi.org/10.1016/j.jastp.2009.09.004

Heki, K., Otsuka, Y., Choosakul, N., Hemmakorn, N., Komolmis, T., & Maruyama, T. (2006). Detection of ruptures of Andaman fault segments in the 2004 great Sumatra earthquake with coseismic ionospheric disturbances. *Journal of Geophysical Research*, *111*(B9), B09313. https://doi.org/10.1029/2005jb004202

Inchin, P., Heale, C., Snively, J., & Zettergren, M. (2020). The dynamics of nonlinear atmospheric acoustic-gravity waves generated by tsunamis over realistic bathymetry. *Journal of Geophysical Research: Space Physics*, *125*(12), e2020JA028309. https://doi.org/10.1029/2020ja028309

Iyemori, T., Nose, M., Han, D., Gao, Y., Hashizume, M., Choosakul, N., et al. (2005). Geomagnetic pulsations caused by the Sumatra earthquake on December 26, 2004. *Geophysical Research Letters*, *32*(20), L20807. https://doi.org/10.1029/2005gl024083

Kanamori, H., Mori, J., & Harkrider, D. G. (1994). Excitation of atmospheric oscillations by volcanic eruptions. *Journal of Geophysical Research*, *99*(B11), 21947–21961. https://doi.org/10.1029/94jb01475

King, J., & Papitashvili, N. (2005). Solar wind spatial scales in and comparisons of hourly Wind and ACE plasma and magnetic field data. *Journal of Geophysical Research*, *110*(A2), A02104. https://doi.org/10.1029/2004ja010649

Lin, Z., Toh, H., & Minami, T. (2021). Direct comparison of the tsunami-generated magnetic field with sea level change for the 2009 Samoa and 2010 Chile tsunamis. *Journal of Geophysical Research: Solid Earth*, *126*(11), e2021JB022760. https://doi.org/10.1029/2021jb022760

Lockwood, M. (2022). *Solar wind-magnetosphere coupling functions: Pitfalls, limitations and applications*. Space Weather. e2021SW002989.

Lognonné, P., Clévédé, E., & Kanamori, H. (1998). Computation of seismograms and atmospheric oscillations by normal-mode summation for a spherical Earth model with realistic atmosphere. *Geophysical Journal International*, *135*(2), 388–406. https://doi.org/10.1046/j.1365-246x.1998.00665.x

Love, J. J., & Chulliat, A. (2013). An international network of magnetic observatories. *Eos, Transactions—*, *94*(42), 373–374. https://doi.org/10.1002/2013eo420001

Manoj, C., Maus, S., & Chulliat, A. (2011). Observation of magnetic fields generated by Tsunamis. *Eos, Transactions American Geophysical Union*, *92*(2), 13–14. https://doi.org/10.1029/2011eo020002

Manoj, C., Maus, S., Lühr, H., & Alken, P. (2008). Penetration characteristics of the interplanetary electric field to the daytime equatorial ionosphere. *Journal of Geophysical Research*, *113*(A12). https://doi.org/10.1029/2008ja013381

Matsumura, M., Saito, A., Iyemori, T., Shinagawa, H., Tsugawa, T., Otsuka, Y., et al. (2011). Numerical simulations of atmospheric waves excited by the 2011 off the Pacific coast of Tohoku Earthquake. *Earth Planets and Space*, *63*(7), 885–889. https://doi.org/10.5047/eps.2011.07.015

Matsumura, M., Shinagawa, H., & Iyemori, T. (2012). Horizontal extension of acoustic resonance between the ground and the lower thermosphere. *Journal of Atmospheric and Solar-Terrestrial Physics*, *75*, 127–132. https://doi.org/10.1016/j.jastp.2011.12.003

Matzka, J., Bronkalla, O., Kervalishvili, G., Rauberg, J., Stolle, C., & Yamazaki, Y. (2022). Geomagnetic Hpo index. V. 2.0. [dataset]. GFZ Data Services. https://doi.org/10.5880/Hpo.0002

Matzka, J., Stolle, C., Yamazaki, Y., Bronkalla, O., & Morschhauser, A. (2021). The geomagnetic Kp index and derived indices of geomagnetic activity. *Space Weather*, *19*(5), e2020SW002641. https://doi.org/10.1029/2020sw002641

McPherron, R. L. (2005). Magnetic pulsations: Their sources and relation to solar wind and geomagnetic activity. *Surveys in Geophysics*, *26*(5), 545–592. https://doi.org/10.1007/s10712-005-1758-7

Meng, X., Vergados, P., Komjathy, A., & Verkhoglyadova, O. (2019). Upper atmospheric responses to surface disturbances: An observational perspective. *Radio Science*, *54*(11), 1076–1098. https://doi.org/10.1029/2019rs006858

Minami, T. (2017). Motional induction by tsunamis and ocean tides: 10 years of progress. *Surveys in Geophysics*, *38*(5), 1097–1132. https://doi.org/10.1007/s10712-017-9417-3

Minami, T., Toh, H., & Tyler, R. H. (2015). Properties of electromagnetic fields generated by tsunami first arrivals: Classification based on the ocean depth. *Geophysical Research Letters*, *42*(7), 2171–2178. https://doi.org/10.1002/2015gl063055

Nakashima, Y., Heki, K., Takeo, A., Cahyadi, M. N., Aditiya, A., & Yoshizawa, K. (2016). Atmospheric resonant oscillations by the 2014 eruption of the Kelud volcano, Indonesia, observed with the ionospheric total electron contents and seismic signals. *Earth and Planetary Science Letters*, *434*, 112–116. https://doi.org/10.1016/j.epsl.2015.11.029

NOAA National Geophysical Data Center. (2009). ETOPO1 1 Arc-minute global Relief model. NOAA National Centers for Environmental Information [dataset]. https://doi.org/10.7289/V5C8276M

Nose, M., Iyemori, T., Sugiura, M., Kamei, T., & World Data Center for Geomagnetism, Kyoto. (2015). Geomagnetic dst index [dataset]. NiCT. https://doi.org/10.17593/14515-74000

Papitashvili, N. E., & King, J. H. (2020). OMNI 1-min data set [dataset]. NASA Space Physics Data Facility. https://doi.org/10.48322/45bb-8792

Richmond, A. D. (1995). Ionospheric electrodynamics. *Handbook of atmospheric electrodynamics*, *2*, 249–290.

Saito, A., Tsugawa, T., Otsuka, Y., Nishioka, M., Iyemori, T., Matsumura, M., et al. (2011). Acoustic resonance and plasma depletion detected by GPS total electron content observation after the 2011 off the Pacific coast of Tohoku Earthquake. *Earth Planets and Space*, *63*(7), 863–867. https://doi.org/10.5047/eps.2011.06.034

Saito, T. (1969). Geomagnetic pulsations. *Space Science Reviews*, *10*(3), 319–412. https://doi.org/10.1007/BF00203620

Schnepf, N., Manoj, C., An, C., Sugioka, H., & Toh, H. (2016). Time–frequency characteristics of tsunami magnetic signals from four Pacific ocean events. In *Global tsunami science: Past and future, volume I* (pp. 3935–3953). Springer. https://doi.org/10.1007/978-3-319-55480-8_14

Shinagawa, H., Iyemori, T., Saito, S., & Maruyama, T. (2007). A numerical simulation of ionospheric and atmospheric variations associated with the Sumatra earthquake on December 26, 2004. *Earth Planets and Space*, *59*(9), 1015–1026. https://doi.org/10.1186/bf03352042

Smart, D. (2022). The first hour of the paroxysmal phase of the 2022 Hunga Tonga–Hunga Ha'apai volcanic eruption as seen by a geostationary meteorological satellite. *Weather*, *77*(3), 81–82. https://doi.org/10.1002/wea.4173

Sorokin, V., & Yaschenko, A. (2021). Generation of magnetic field in the low-latitude ionosphere by tsunami wave. *Journal of Atmospheric and Solar-Terrestrial Physics*, *213*, 105521. https://doi.org/10.1016/j.jastp.2020.105521

Tahira, M. (1995). Acoustic resonance of the atmospheric at 3.7 mHz. *Journal of the Atmospheric Sciences*, *52*(15), 2670–2674. https://doi.org/10.1175/1520-0469(1995)052<2670:arotaa>2.0.co;2

Torrence, C., & Compo, G. P. (1998). A practical guide to wavelet analysis. *Bulletin of the American Meteorological Society*, *79*(1), 61–78. https://doi.org/10.1175/1520-0477(1998)079<0061:apgtwa>2.0.co;2

Yamazaki, Y., Matzka, J., Stolle, C., Kervalishvili, G., Rauberg, J., Bronkalla, O., et al. (2022). Geomagnetic activity index Hpo. *Geophysical Research Letters*, *49*(10), e2022GL098860. https://doi.org/10.1029/2022gl098860

Yamazaki, Y., & Maute, A. (2017). Sq and EEJ–A review on the daily variation of the geomagnetic field caused by ionospheric dynamo currents. *Space Science Reviews*, *206*(1), 299–405. https://doi.org/10.1007/s11214-016-0282-z

Yeh, K. C., & Liu, C. H. (1974). Acoustic-gravity waves in the upper atmosphere. *Reviews of Geophysics*, *12*(2), 193–216. https://doi.org/10.1029/rg012i002p00193

Yuen, D. A., Scruggs, M. A., Spera, F. J., Zheng, Y., Hu, H., McNutt, S. R., et al. (2022). Under the surface: Pressure-induced planetary-scale waves, volcanic lightning, and gaseous clouds caused by the submarine eruption of Hunga Tonga-Hunga Ha'apai volcano provide an excellent research opportunity. *Earthquake Research Advances*, 100134. https://doi.org/10.1016/j.eqrea.2022.100134

Zettergren, M., & Snively, J. (2013). Ionospheric signatures of acoustic waves generated by transient tropospheric forcing. *Geophysical Research Letters*, *40*(20), 5345–5349. https://doi.org/10.1002/2013gl058018

Zettergren, M., & Snively, J. (2015). Ionospheric response to infrasonic-acoustic waves generated by natural hazard events. *Journal of Geophysical Research: Space Physics*, *120*(9), 8002–8024. https://doi.org/10.1002/2015ja021116

Zettergren, M., & Snively, J. (2019). Latitude and longitude dependence of ionospheric TEC and magnetic perturbations from infrasonic-acoustic waves generated by strong seismic events. *Geophysical Research Letters*, *46*(3), 1132–1140. https://doi.org/10.1029/2018gl081569